Nuclear Instruments and Methods in Physics Research A 1060 (2024) 169067

Contents lists available at ScienceDirect

Nuclear Inst. and Methods in Physics Research, A

journal homepage: www.elsevier.com/locate/nima

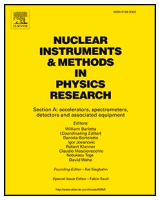

Experimental validation of Monte Carlo NaI(Tl) detector efficiency responses with surrogate ^{137}Cs environmental contamination source term

E. Asano , S.A. Dewji *

Nuclear and Radiological Engineering and Medical Physics Programs, George W. Woodruff School of Mechanical Engineering, Georgia Institute of Technology, Atlanta, GA, 30332-0405, USA

ARTICLE INFO

Keywords:
Gamma spectrometry
NaI(Tl) detector
Radiation transport
Monte Carlo
Environmental contamination

ABSTRACT

Radiological site remediation is a resource intensive process requiring extensive field sampling to demonstrate regulatory compliance. Specifically, the application of Monte Carlo (MC) simulations and automated hybrid radiation transport methods has garnered interest in streamlining the remediation process by simulating detector responses for a plurality of contaminated media, contamination depths and profiles, and source-detector orientations. In this study, experimental validation of gamma-ray detector efficiency responses was conducted for simulations of radiological site-specific and idealized external contamination conditions. Measurements were performed with a cylindrical 2″ × 2″ sodium iodide thallium-doped (NaI(Tl)) scintillator detector suspended above a 217.8 kBq, 50 cm × 50 cm ^{137}Cs contamination source located on the surface of or buried within environmental soil. New area correction factors (ACFs) and gamma shielding factors (GSFs) were also derived to modify the simulated idealized detector efficiency responses, accounting for reductions in source area and clean soil covering layers, respectively, that may be encountered when performing *in-situ* gamma spectrometry in the field. The study concluded that simulated total detection efficiency from energy deposition in the active volume of the detector crystal can be adopted for radionuclide screening purposes. Furthermore, pragmatic implementation of environmental surveying using gamma-spectrometry requires site-specific information.

1. Introduction

The radiological site remediation process is a long-term, costly, and complex endeavor that may be facilitated with the use of radiation transport tools. Radiation transport tools may be harnessed to reproduce gamma-ray detector responses measured in the field to facilitate sampling and laboratory analysis efforts required to demonstrate regulatory compliance during the remediation of radiologically contaminated sites [1,2]. The use of Monte Carlo (MC) radiation transport simulations, combined with fully automated hybrid radiation transport methods, has been recently explored for a plurality of environmental contamination media, gamma-ray emitting radionuclides, and source-detector orientations [3]. The utility of radiation transport variance reduction methods (VR) methods has additionally explored the efficiency, accuracy, and reliability (collectively referred to as “effectiveness”) when estimating MC energy deposition-based total detector efficiency responses (activity-normalized detector count rate, summed over the entire spectrum), which may ultimately be used for demonstrating regulatory compliance in the radiological site remediation process [1,2]. In essence, real-time detector readings (i.e., in Counts-Per-Minute, CPM) in the field may be compared to simulated responses derived from pre-determined dose- or carcinogenic risk-based regulatory limits (i.e., radionuclide concentrations in environmental media) when surveying contaminated sites. In prior simulation-based work, total detector efficiencies were estimated for a breadth of environmental contamination scenarios by combining capabilities of the pulse height tally (PHT) and Consistent Adjoint Driven Importance Sampling (CADIS) hybrid radiation transport method [4,5] offered by the Monte Carlo N-Particle (MCNP) [6] and Shift [7,8] codes, respectively. However, experimental validation of simulated detector efficiency responses was still required to evaluate the utility of applying MC energy deposition-based detector efficiencies to realistic field surveying environments.

In this study, laboratory measurements were performed with a cylindrical 2″ × 2″ sodium iodide thallium-doped (NaI(Tl)) scintillating gamma-ray detector suspended at varying distances above soil contaminated with a 217.8 kBq ^{137}Cs planar source of 50 cm × 50 cm in dimension (custom embedded between 0.127 mm thick plastic films; uniform source contamination was assumed), located on or beneath the

* Corresponding author.
E-mail address: shaheen.dewji@gatech.edu (S.A. Dewji).

https://doi.org/10.1016/j.nima.2023.169067
Received 1 November 2023; Received in revised form 4 December 2023; Accepted 26 December 2023
Available online 29 December 2023

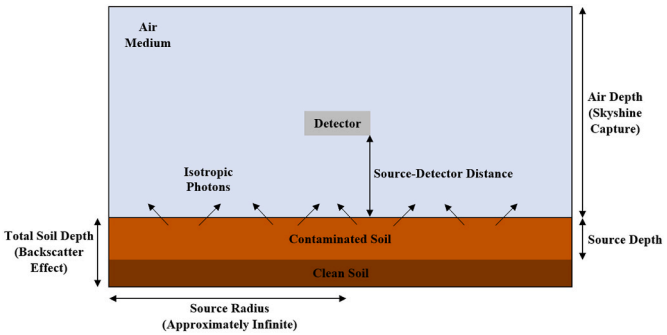

Fig. 1. Sample idealized soil contamination model (*not to scale*).

soil surface. The source is intended to be a representative field surrogate source term that may be encountered when performing *in-situ* gamma-ray measurements at a contaminated site, representing contamination in environmental media. From a simulation perspective, the models of interest in this study are assumed to be idealized, meaning that source regions are effectively infinite in lateral extent with uniform radionuclide concentrations [9]. The source regions are also assumed to be free of any overlaying layers of clean soil. Inconsistencies between idealized and real-world exposure conditions in the field may thus lead to highly inaccurate estimates of dose/carcinogenic risk at a contaminated site. Hence, new sets of area correction factors (ACFs) [10] and gamma shielding factors (GSFs) [11] need to be derived to modify simulated detector efficiencies for use in future radiological site remediation applications. In addition to reduced source area and clean cover soil thickness, the idealized models do not account for many other real-world field nuances (e.g., ground roughness) [12]. Accordingly, the capabilities and limitations of using MC energy deposition-based detector efficiencies for relating detector readings in the field to dose- or risk-based radionuclide concentrations are also identified through experimental validation of simulated detector efficiencies in this study.

1.1. Background

In past decades, *in-situ* gamma spectrometry has been utilized to ultimately relate detector readings back to more meaningful quantities such as dose from external exposure to radionuclides concentrated in environmental media. In particular, the external exposure pathway is often the most significant contributor to the overall dose when compared to other exposure pathways [13]. *In-situ* gamma spectrometry was utilized in early studies that sought to estimate levels of exposure from fallout in soil following the resumption of atmospheric nuclear weapons testing in the 1960s [14–16]. In the years following, there was a renewed interest in harnessing *in-situ* gamma spectrometry for rapid assessments of radionuclide activity concentrations in soil following the Three Mile Island/Chernobyl reactor accident [17–20]. Recently, *in-situ* gamma spectrometry has been investigated for facilitation of future large-scale radiological site remediation applications [3,4].

In the radiological site remediation process, prior to stakeholders deciding upon site release for restricted or unrestricted use, regulatory compliance below a dose- or carcinogenic risk-based regulatory limit must be successfully demonstrated [2]. Given that the average time is three years for radiological site cleanup [13], sample collection and laboratory analyses efforts required to demonstrate regulatory compliance may become resource intensive and time-consuming. Although sample collection and laboratory analyses efforts are inevitably required to demonstrate regulatory compliance in site remediation [1,2], these efforts may be greatly reduced with so-called "calibration factors" that directly relate detector readings to radionuclide concentrations in environmental media.

Calibration factors have traditionally been generated using semi-empirical methods, which required knowledge of the spectral distribution of the measured photon fluence [19,20]. While useful for assessing complex radionuclide inventories, numerous limitations are inherent to these semi-empirical methods, such as the following: (a) random and systematic errors from measurements, along with uncertainties associated with analytical calculations are introduced (b) use of the full energy peak (i.e., rather than the total); detector efficiency may require extensive source counting times to achieve reliable counting statistics, especially when contamination levels do not greatly exceed background; and (c) in large-scale, wide-area contamination applications, calibration factor production may quickly become cumbersome as the number of required measurements increases.

2. Methodology

In this section, we describe the methodical approach that was adopted to validate simulated detector efficiencies with field surrogate source term measurements in the Radiological Engineering, Detection, and Dosimetry (RED^2) Laboratory at the Georgia Institute of Technology. The study addresses the measurement/simulation conditions, associated assumptions, and concludes with metrics of comparison used for validation of simulated results.

To address limitations of prior semi-empirical methods for generating calibration factors and ultimately complement sample collection and laboratory analyses efforts in wide-area contamination applications, a compendium of MC-based calibration factors was recently generated in a massive modeling research effort [3]. The calibration factors were generated for thousands of idealized, wide-area contamination scenarios based on the following modeling parameters: (a) NaI(Tl) detector configuration; (b) source-detector distance; (c) monoenergetic gamma-ray source energy; (d) contaminated medium type; and (e) source depth profile (located along the surface or distributed volumetrically throughout a medium) [3]. An idealized model example is depicted in Fig. 1; principally, idealized models serve as baseline exposure scenarios that may be modified based on available site-specific information when deriving regulatory limits. For additional clarification, a flow chart outlining how calibration factors may be implemented in the radiological site remediation process is depicted in Fig. 2.

Within the prior modeling research effort, energy deposition-based total detector efficiencies (normalized to obtain calibration factors) were estimated using only MCNP for surface sources, whereas all distributed source responses were estimated using the so-called "Shift with CADIS method" [21]. The Shift with CADIS method was developed to essentially exploit the accelerated cell flux capability offered by Shift, along with a unique detector response function (DRF) implementation to interpolate over the MCNP surface source responses and, ultimately, yield distributed source responses. Further details of the methodology may be found in the literature [3]. Although simulated detector efficiencies have been rigorously verified [4], an experimental validation was still required to demonstrate the field utility of these radiation transport-based models.

This study presents a methodology for experimentally validating MC-based detector efficiencies (inclusive of total and full energy peak detector efficiencies) that may be used to ultimately relate detector readings in the field to dose/carcinogenic risk. Through experimental validation of simulated results, the potential for in-situ gamma spectrometry as an "independent characterization tool" [21] may be further increased. This methodology further assumes that the radionuclides of interest have already been identified, necessitating further field sampling through the methods and validation presented in this study.

2.1. Experimental setup, energy calibration, and background acquisition

A Mirion model NAIS-2 × 2 (SN 13006086) NaI(Tl) scintillation detector [22] combined with an Osprey (SN 13004001) digital multi-channel analyzer (MCA) tube base [23] and Mirion Genie 2000 gamma acquisition software [24] was utilized for all counting

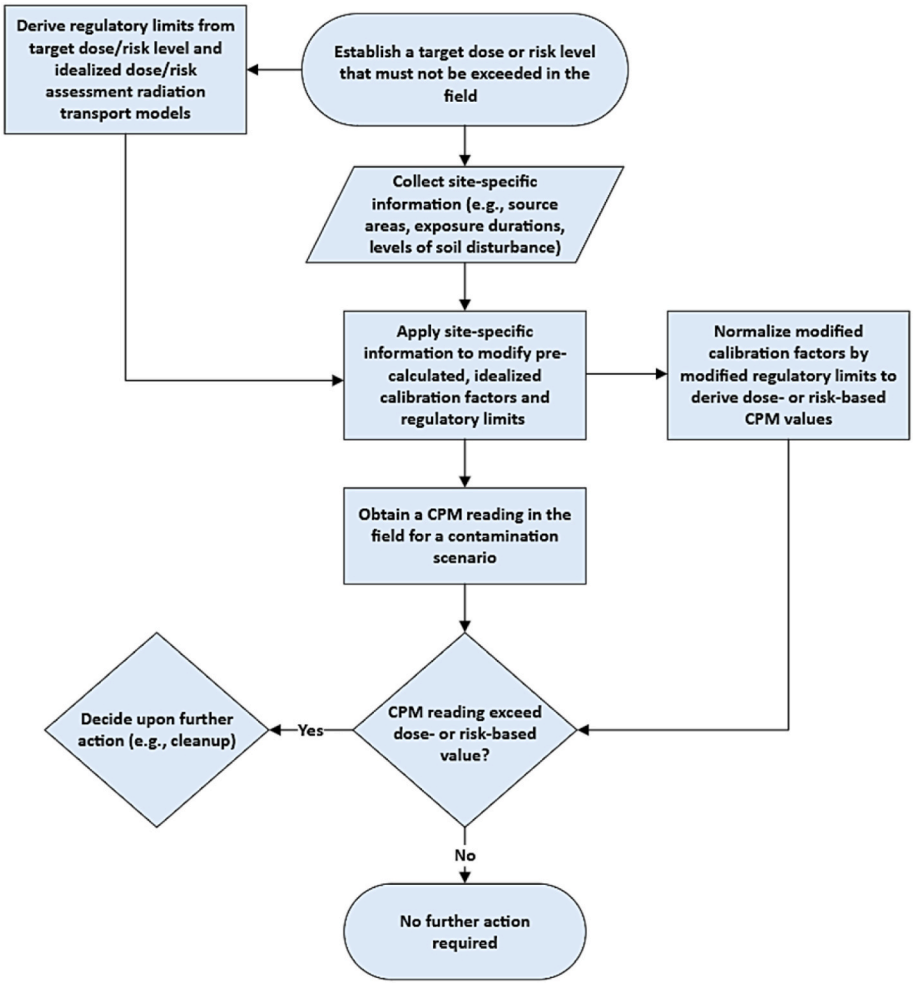

Fig. 2. Flow chart depicting the implementation of calibration factors for ultimately demonstrating regulatory compliance in the radiological site remediation process.

Table 1
Summary of calibration source specifications.

Source	Activity (μCi)	Calibration Date	Half-Life (yr)	Peak Energy (keV)	Centroid Channel
^{22}Na	1.06	09/08/2022	2.60	511	182
^{137}Cs	0.97	09/08/2022	30.08	661.7	232
^{54}Mn	0.91	02/01/2023	0.86	835	291
^{60}Co	1.00	09/08/2022	5.27	1173.2	404
				1332.5	458

measurements. The detector was energy-calibrated by associating each channel number with the energy of a known source using NIST-calibrated reference sources [25] from Table 1, resulting in a 3000 keV calibrated spectrum over 1024 channels.

For the experimental setup, a 3 ft × 4 ft × 2 ft (91.44 cm × 121.92 cm × 60.96 cm) deep aluminum box was filled with Timberline organic topsoil (UPC #: 742786911087) up to 4.5 cm from the top of the aluminum box. Extensive efforts were made to ensure that the soil was evenly distributed throughout the box (i.e., to emulate an idealized soil medium) by dispersing and re-distributing hardened clumps. The precise composition of the soil was unknown but was determined to be insignificant, given that mass attenuation coefficients of soil are insensitive to the elemental composition above 200 keV [26]. This assumption is valid for the current study since the most prominent emission of the measured ^{137}Cs source is 662 keV, which occurs with an emission probability of 89.7 % from the decay of ^{137m}Ba, and which also represents an EPA Superfund radionuclide of interest [27].

The bulk density of the soil was approximated by filling a cylindrical five-gallon (18.9 L) plastic bucket with the soil and using a hanging scale to obtain a value of approximately 0.47 g/cm^3. The detector was placed in a laboratory extension clamp and suspended above the center of the soil surface at varying distances.

2.2. Field surrogate source term acquisition

A 217.8 kBq ^{137}Cs 50 cm × 50 cm planar source (SRS 126055) was centered along the soil surface or at a prescribed depth within the soil for a newly fabricated source. Fig. 3 displays a surface source contamination scenario with a source-detector distance of 1 cm, along with the background acquisition setup for comparison. Source centering and depth locations were marked within the aluminum box, and a shovel was frequently used to excavate and re-distribute soil when constructing the buried sources. In total, 12 measurements were performed, inclusive of three source-detector distances (1 cm, 10 cm, and 30 cm) and four planar source depths (surface, 1 cm, 15 cm, and 32 cm). Counting time was implemented for all measurements to achieve an uncertainty (fractional standard deviation of the net count rate at 1 σ) of less than 5 %.

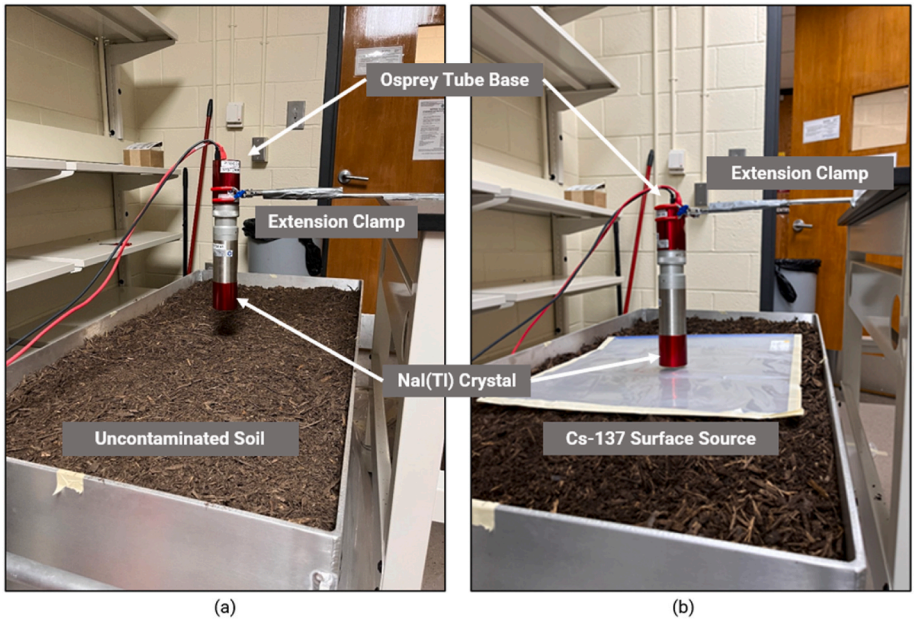

Fig. 3. (a) Background and (b) example source acquisition setups.

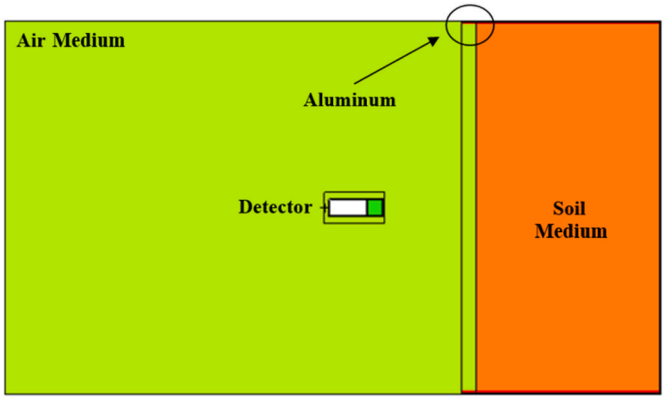

Fig. 4. Sample source acquisition model rendering from the MCNP Visual Editor.

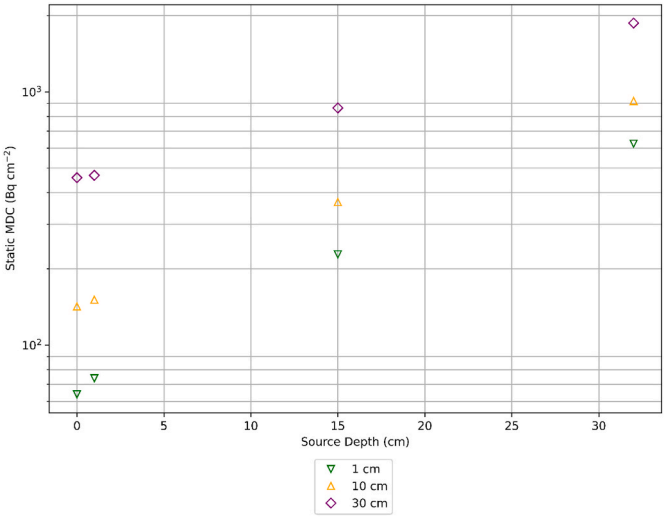

Fig. 5. Calculated static MDCs as a function of planar source depth in soil for each source-detector distance.

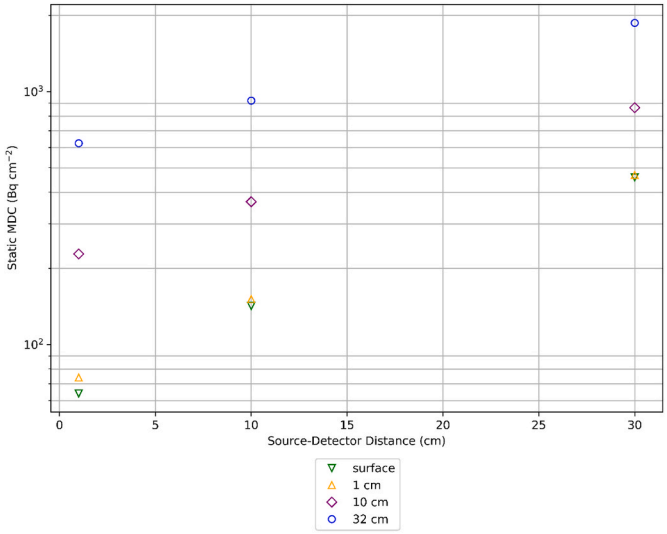

Fig. 6. Calculated static MDCs as a function of source-detector distance for each planar source depth in soil.

2.3. Metrics of comparison

All metrics of comparison involve validations of simulated total or full energy peak detector efficiencies (normalized to count rates) with measured counterparts. Total and full energy peak efficiencies were included in the validation effort since either response may be related to radionuclide concentrations in environmental media, and thus dose or carcinogenic risk when demonstrating regulatory compliance at a contaminated site. Validation of the total detector efficiency is of primary interest in this study due to its potential utility in facilitating future radiological site remediation efforts, as previously described in Section 1. The total detector efficiency, ε_{total}, in its most generic form is given as

$$\varepsilon_{total} = \frac{Net\ Count\ Rate\ \left(\frac{counts}{s}\right)}{Source\ Activity\ \left(\frac{decays}{s}\right) \times Yield\ \left(\frac{photons}{decay}\right)}. \quad (1)$$

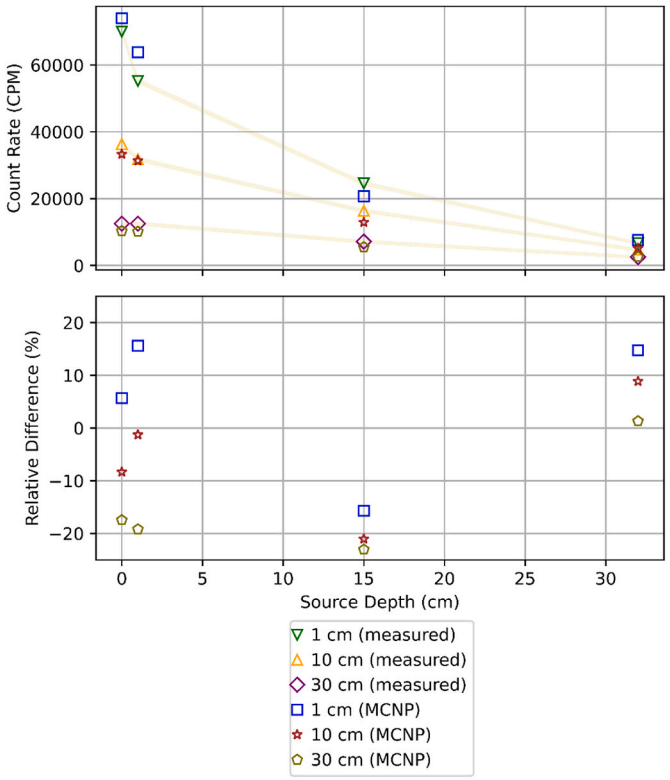

Fig. 7. Measured and simulated planar source responses for ^{137}Cs as a function of source depth in soil for each source-detector distance. Relative percent differences between simulated responses and measured counterparts are also provided.

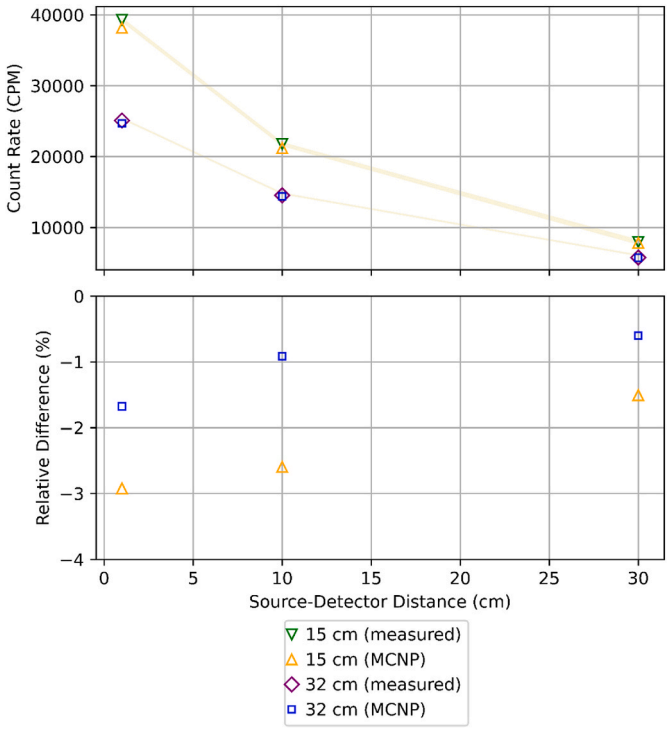

Fig. 8. Measured and simulated distributed source responses for ^{137}Cs as a function of source-detector distance for each source depth in soil. Relative percent differences between simulated responses and measured counterparts are also provided.

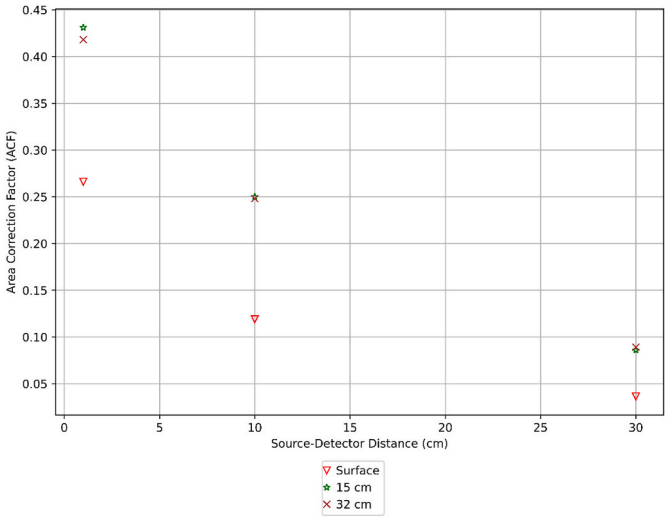

Fig. 9. Cs-137 ACFs as a function of source-detector distance for the planar surface source and each distributed source depth in soil.

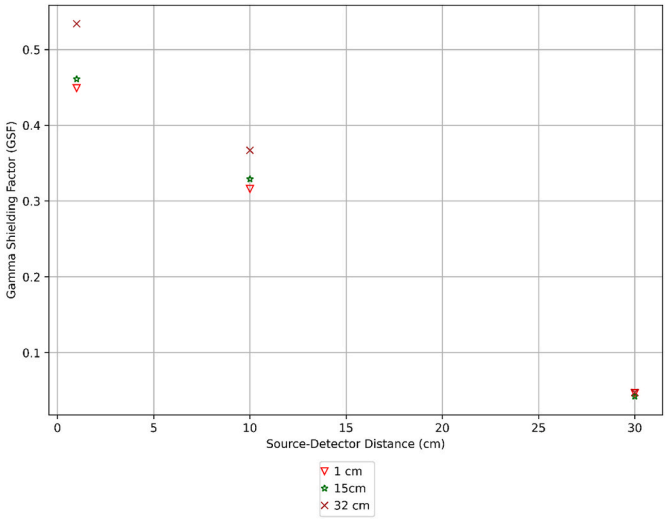

Fig. 10. Cs-137 GSFs as a function of source-detector distance for each planar source depth in soil.

It is worth noting that Eq. (1) may be broken down further into components that explicitly account for dependencies such as source-detector distance, attenuation throughout intervening materials, self-attenuation, and the interaction probability of the detection material [28]. The numerator of Eq. (1) considers all partial (e.g., Compton continuum) and full (i.e., photoelectric absorption) energy deposition events within the detector crystal. Full energy deposition events that register within the detection system may produce a photopeak, which is a highly useful spectrum component for radionuclide identification purposes. The full energy peak detector efficiency, ε_{peak}, associated with all (registered) full energy deposition events is related to Eq. (1) as shown below:

$$\varepsilon_{peak} = \varepsilon_{total} \times \left(\frac{Photopeak\ Counts}{Net\ Counts} \right). \quad (2)$$

2.3.1. Planar source Monte Carlo detector responses

In addition to validating simulated detector efficiencies estimated from idealized models, the experimental setup was also reproduced using MCNP to obtain direct comparisons with measured responses. For

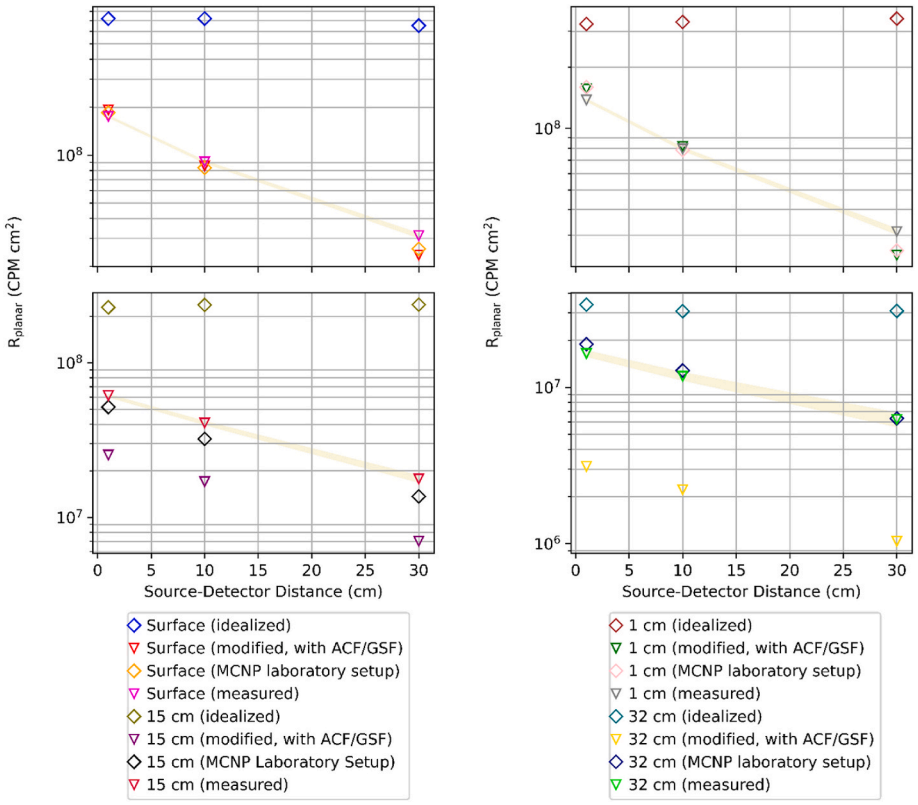

Fig. 11. Planar ^{137}Cs source responses for each case as a function of source-detector distance for each source depth in soil.

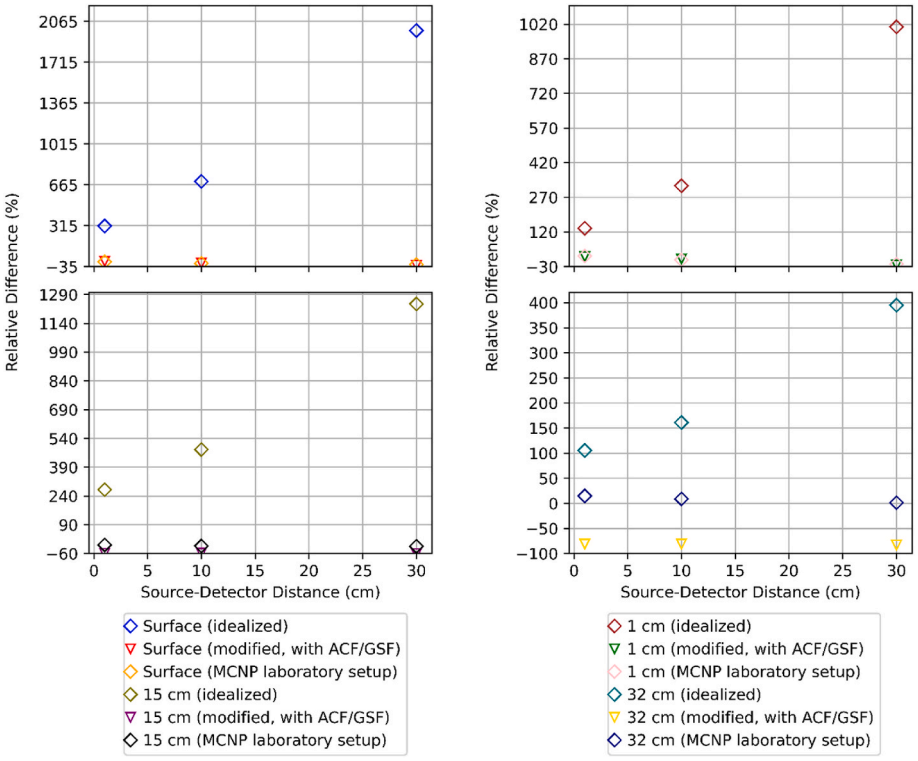

Fig. 12. Relative percent differences of ^{137}Cs planar source responses with respect to measured counterparts for each case as a function of source-detector distance for each source depth in soil.

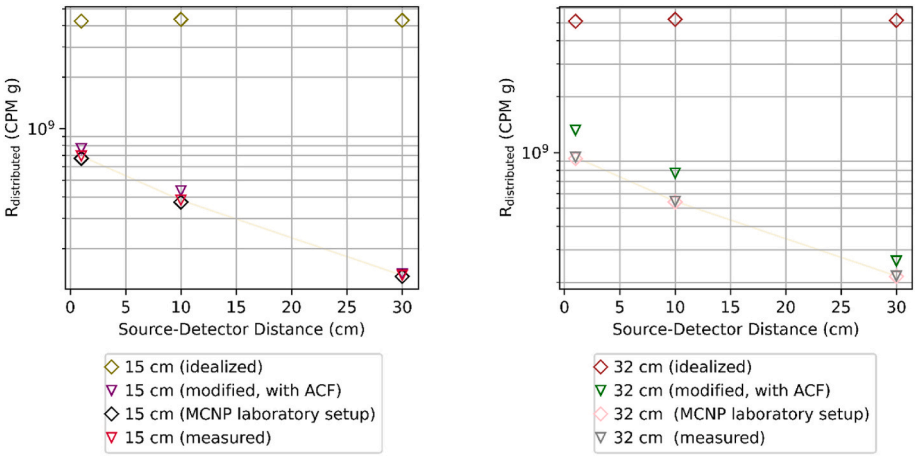

Fig. 13. Distributed ^{137}Cs source responses for each case as a function of source-detector distance for each source depth in soil.

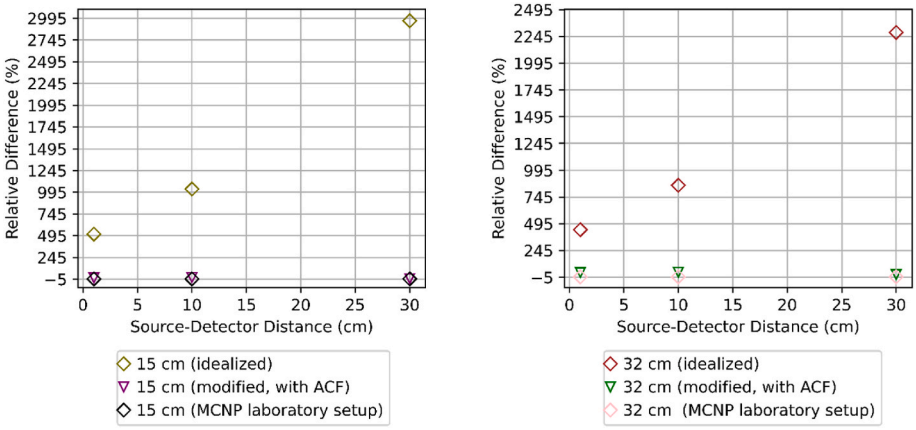

Fig. 14. Relative percent differences of ^{137}Cs distributed source responses with respect to measured counterparts for each case as a function of source-detector distance for each source depth in soil.

all MCNP simulations in the current study, photon transport was simulated using the detailed physics treatment interaction model (i.e., accounting for coherent scattering, fluorescence, and electron binding effects) [6]. Bremsstrahlung generation, however, was simulated using the simple physics treatment (i.e., thick-target bremsstrahlung (TTB)) interaction model [6]. A sample rendering of an experimental setup model from the MCNP Visual Editor [29] is provided in Fig. 4.

Integrated pulse heights estimated with MCNP were normalized as follows to obtain a net count rate as CPM:

$$Net\ Count\ Rate_{MCNP}\left(\frac{counts}{min}\right) = Pulse\ Height\left(\frac{counts}{Bq-s}\right) \times Source\ Activity\ (Bq) \times \left(\frac{60\ s}{min}\right) \quad (3)$$

To ensure consistency with measurements, the measured spectrum energy bin structure was replicated in MCNP. A simplified Mirion Model 802 [30] 2″ × 2″ NaI(Tl) detector was constructed in MCNP. Although simulated and experimental detector models differ, the analysis was considered valid since the crystal dimensions and overall structures are nearly identical [31]. For all MCNP simulations, silty soil [20] elemental composition was assumed, and the density was defined as 0.47 g/cm^3 to replicate the measured value.

Measured net count rates were calculated through simple subtraction of the measured background count rate from the source count rates. Measured net count rate uncertainties were propagated, and relative percent differences between MCNP and measured net count rates were ultimately used as a metric for assessing levels of convergence.

2.3.2. *Distributed source Monte Carlo detector responses*

Distributed source measurements in the field are of particular concern in the radiological site remediation process due to the possibility of migration to the groundwater exposure pathway [13]. Exposure areas with significantly high levels of contamination (i.e., “hot spots”) at the soil surface may be used to delineate regions to target for subsurface sampling [13], where various source depth profiles may be assumed. Due to the potential for groundwater contamination and often extensive amounts of distributed source contamination scenarios encountered in the field, accurate simulation of detector responses is needed to effectively facilitate sampling and analyses efforts.

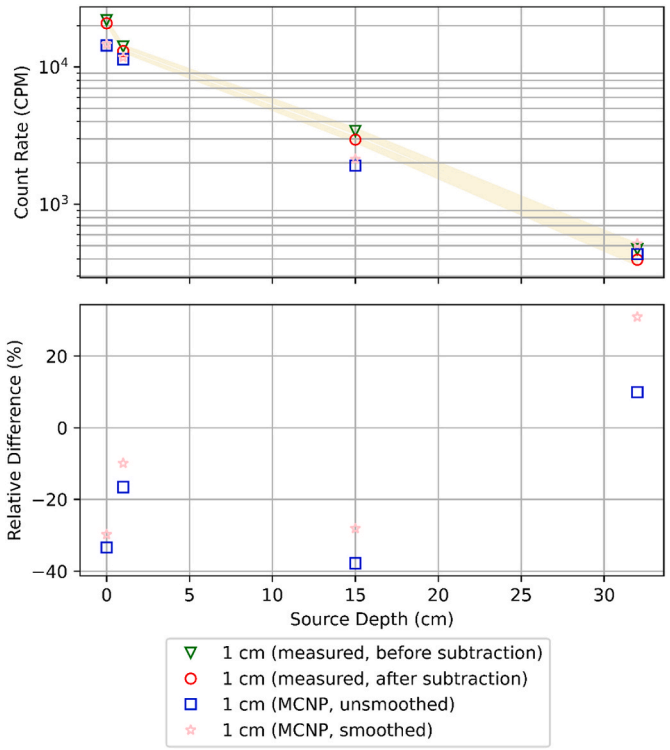

Fig. 15. Measured and simulated full energy peak responses for ^{137}Cs as a function of planar source depth in soil for the 1 cm source-detector distance. Corresponding relative differences between MCNP (smoothed) responses and measured counterparts before and after Compton continuum subtraction are also displayed.

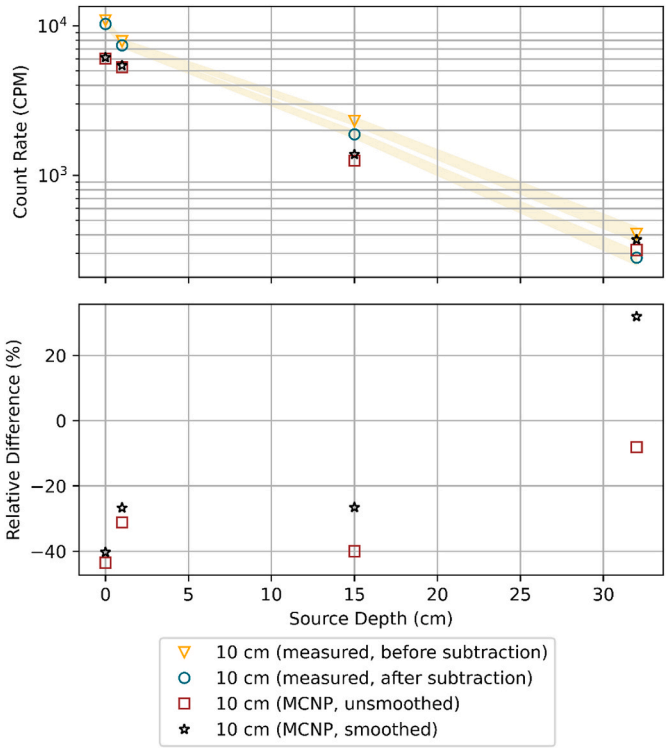

Fig. 16. Measured and simulated full energy peak responses for ^{137}Cs as a function of planar source depth in soil for the 10 cm source-detector distance. Corresponding relative differences between MCNP (smoothed) responses and measured counterparts before and after Compton continuum subtraction are also displayed.

Net count rates from distributed source measurements were approximated analytically as

$$CR_{net}(E) = \frac{1}{\mu}\int_0^{\mu L} f(E,\tau)d\tau, \tag{4}$$

where $CR_{net}(E)$ is the energy-dependent, net count rate from a uniformly distributed source of depth τ in number of mean-free paths (MFPs), with μ (cm^{-1}) and L (cm) being the linear attenuation coefficient and extent of the source (extending from the air-ground interface down to a prescribed depth), respectively. A function $f(E,\tau)$ was constructed for each of the three source-detector distances, with each consisting of the net count rate responses for all buried planar source depths (1 cm, 15 cm, and 32 cm). Ultimately, each function was integrated over τ within Eq. (4) to approximate measured distributed source net count rates for 15 cm and 32 cm source depths at each source-detector distance. To approximate uncertainties associated with Eq. (4), the MC method was implemented by the following steps:

1. Parameters of $f(E,\tau)$ (i.e., planar source count rates with known uncertainties) were sampled from a normal distribution using a sample size of 10,000 for each source-detector distance and distributed source depth profile;
2. Piecewise cubic hermite interpolating polynomial (PCHIP) interpolation [32] was then used to reconstruct the 10,000 $f(E,\tau)$ functions from the newly sampled parameters; and
3. All reconstructed $f(E,\tau)$ functions were integrated using Eq. (4), and the uncertainties were ultimately approximated from the integrated results.

2.3.3. *Validation of idealized simulations*

Idealized total detector efficiency responses were normalized to net count rate responses and benchmarked with measured and simulated MCNP laboratory setup counterparts. Although, contrary to the former and latter counterparts, the idealized responses were derived from infinitely wide source transport models without any additional layers of clean soil covering the source. For direct comparison with measured and simulated MCNP laboratory setup responses, new ACFs and GSFs were derived and normalized to the idealized responses. ACFs and GSFs have traditionally been used by the EPA to modify idealized dose- or carcinogenic risk-based regulatory limits when encountering source area reductions and additional layers of clean soil covering in the field, respectively [13]. Normalization of site-specific regulatory limits by idealized calibration factors (see Fig. 2), however, result in overly conservative dose- or risk-based CPM responses. It is this subtlety that motivated the need for newly derived ACFs and GSFs (regulatory limits should, however, still be normalized by currently available ACFs/GSFs).

Currently available ACFs/GSFs are derived from the ratio of air kerma 1 m above the soil for a given source area and thickness to the air kerma 1 m above the soil for an infinitely wide source area and equivalent thickness (dose- and risk-based regulatory limits are both derived from idealized dosimetric models) [10,11]. ACFs for modifying idealized detector response models were instead calculated as

$$ACF_{A,t} = \frac{Pulse\ Height_{A,t} \times Source\ Area_{A,t}}{Pulse\ Height_{\infty,t} \times Source\ Area_{\infty,t}}, \quad (5)$$

where $ACF_{A,t}$ is the ACF for a cylindrical source (consistent with Asano et al. [3]) with area A and thickness t, $Pulse\ Height_{A,t}$ and $Pulse\ Height_{\infty,t}$ are the simulated detector (integrated) pulse heights at source thickness t with area A and infinite area ∞, respectively, and $Source\ Area_{A,t}$ and $Source\ Area_{\infty,t}$ are source areas associated with $Pulse\ Height_{A,t}$ and $Pulse\ Height_{\infty,t}$, respectively. Accordingly, GSFs were calculated as

$$GSF_{A,t} = \frac{Pulse\ Height_{h,t} \times Source\ Area_{\infty}}{Pulse\ Height_{surface,t} \times Source\ Area_{\infty}} = \frac{Pulse\ Height_{h,t}}{Pulse\ Height_{surface,t}}, \quad (6)$$

where $GSF_{A,t}$ is the GSF for a cylindrical source with area A and thickness t, $Pulse\ Height_{h,t}$ is the simulated detector pulse height for an infinitely wide source with thickness t and soil cover thickness h, and $Pulse\ Height_{surface,t}$ is the simulated detector pulse height for an infinitely-wide surface source with thickness t.

It should be noted that ACFs were not calculated for buried planar sources. Additionally, rather than creating additional DRFs and post-processing algorithms per Shift with CADIS to derive the numerator in Eq. (5), $Pulse\ Height_{A,t}$ responses were estimated directly in MCNP with ^{137}Cs emission spectrum data taken from the International Commission on Radiological Protection (ICRP) Publication 107 [33]. For consistency, all remaining variables from Eqs. (5) and (6) were also estimated directly in MCNP using ^{137}Cs emission spectrum data; surface sources were simulated using the DXTRAN [6] VR technique, whereas distributed sources were simulated using reflective boundary conditions accompanied by reduced source radii (approximating full-width infinite source conditions) [34].

For a direct comparison with measured and MCNP laboratory setup detector responses, the $Pulse\ Height_{\infty,t}$ was normalized by the $ACF_{A,t}$ and $GSF_{A,t}$ to yield

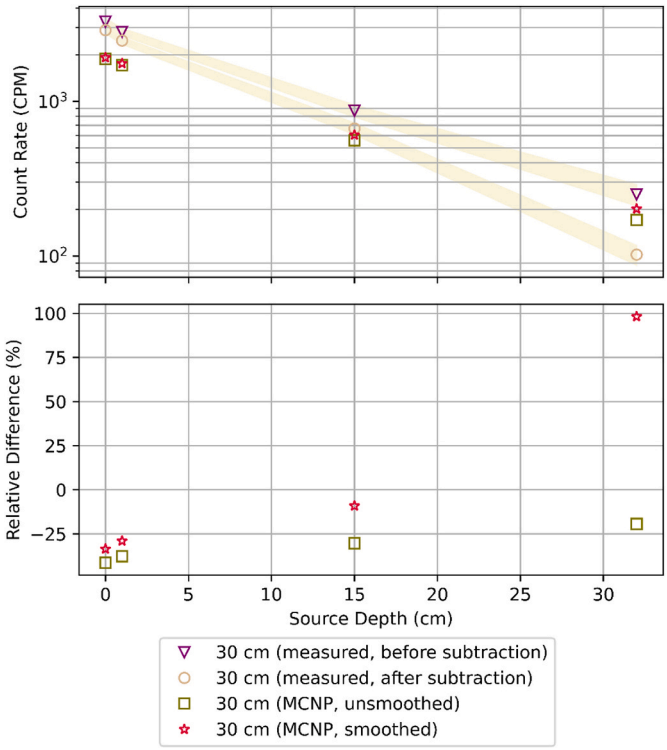

Fig. 17. Measured and simulated full energy peak responses for ^{137}Cs as a function of planar source depth in soil for the 30 cm source-detector distance. Corresponding relative differences between MCNP (smoothed) responses and measured counterparts before and after Compton continuum subtraction are also displayed.

$$R_{planar} = \left[Pulse\ Height_{\infty,t} \times \left(\frac{Source}{Area} \right)_{\infty} \times Source\ Activity\ (Bq) \times \left(\frac{60\ s}{min} \right) \times ACF_{A,t} \times GSF_{A,t} \right] \quad (7)$$

for planar sources and

$$R_{distributed} = \left[Pulse\ Height_{\infty,t} \times \left(\frac{Source}{Area} \right)_{\infty} \times Source\ Depth\ (cm) \times Soil\ Density \left(\frac{g}{cm^3} \right) \times Source\ Activity\ (Bq) \times \left(\frac{60\ s}{min} \right) \times ACF_{A,t} \times GSF_{A,t} \right] \quad (8)$$

for distributed sources, where R_{planar} and $R_{distributed}$ are the modified responses in (CPM cm^2) and (CPM g), respectively, and $\left(\frac{Source}{Area} \right)_{\infty}$ is the infinite (idealized) source area in cm^2.

2.3.4. Validation of full energy peak detector efficiency

Full energy peak detector efficiency responses (normalized to count rates in CPM) were estimated using the MCNP laboratory setup models and validated with measured responses. The Compton continuum from each measured ^{137}Cs photopeak was subtracted, and levels of convergence between simulated and measured photopeak count rates before and after subtraction were observed. This was achieved by establishing a region of interest (ROI) around each measured photopeak and using PCHIP [32] interpolation to obtain the Compton continuum boundary within each ROI. Interpolated count rates along the Compton continuum were then subtracted from corresponding initial count rates and summed across all photopeak ROI measurement points. Uncertainties in the measured photopeak count rates (before and after subtraction) were propagated and reported with the results.

2.3.4.1. Accounting for detector energy resolution in simulated models.

The MCNP PHT bins all photoelectric absorptions into a single energy bin as a delta function by default [35]. To account for statistical fluctuations that occur when registering the incoming photon energy within a detection system, MCNP offers a Gaussian Energy Broadening (GEB) functionality [6] based on full-width-at-half-maximum (FWHM) data as

shown below:

$$FWHM = a + b\sqrt{E + cE^2}, \tag{9}$$

where a, b, and c are user-supplied parameters, and E is the incoming photon energy in MeV. Each parameter may be derived by determining the experimental detector resolution as a function of energy during the energy calibration process and then iteratively fitting the results to Eq. (9). To expedite this process, GEB parameters derived from Dewji et al. [35] were implemented in the current study for smoothing of MCNP PHT spectra to enable direct comparisons with simulated and measured photopeak count rate responses.

2.3.5. Static minimum detectable concentrations (MDCs)

Prior to performing measurements, it is imperative to assess the performance of the detection system to ensure that a given source in the field can be reliably detected. The static minimum detectable concentration (MDC) was calculated for each contamination scenario and used as a metric to assess the performance of the detection system. The static MDC is the *a priori* activity concentration level that an instrument is expected to detect 95 % of the time for a static measurement and is analogous to the well-known minimum detectable activity (MDA) [36]. MDCs were calculated rather than MDAs since we are primarily concerned with relating detector readings to radionuclide concentrations for demonstrating regulatory compliance. Static MDCs were calculated as [36].

$$Static\ MDC\ \left(\frac{Bq}{cm^2}\right) = \frac{3 + 4.65\sqrt{R_B T}}{T\varepsilon_{total} G}, \tag{10}$$

where R_B is the background count rate (CPM), T is the measurement count time (minutes), ε_t is the total detector efficiency, and G is the geometry correction factor (i.e., NaI(Tl) detector crystal area in cm^2). Given that T and G were known beforehand, upon measuring R_B and the soil density in the laboratory, ε_{total} was estimated for each contamination scenario using the MCNP laboratory setup models to derive the static MDCs.

3. Results and discussion

Results associated with total and full energy peak detector efficiency responses are presented and analyzed in Sections 3.1-3.3 and 3.4, respectively. For all numerical results presented hereafter (inclusive of plots/tables associated with MC/analytical calculations), a convergence criterion of 5 % in the relative error (1 σ) was assumed. In addition, 2 σ bounds (i.e., 95 % confidence intervals) surrounding reference results are depicted by (beige) translucent bars in all plots where applicable. Supporting data for all plots are tabulated in Appendix A: Supplementary Data in Tables A.1- A.8.

3.1. Static minimum detectable concentrations (MDCs)

The impact of source depth and source-detector distance on the static MDC for each contamination scenario is shown in Figs. 5 and 6. When examining increases in the static MDC with each incremental increase in source depth and source-detector distance, the impact of each parameter on the static MDC appears significant. Notably, all static MDCs in Figs. 5 and 6 reside well below the measured source activity concentration of 8440 Bq cm^{-2}. We can therefore assume with confidence that all measurements conformed within the performance limits of the detector.

3.2. Comparison to MCNP laboratory setup models

Planar source responses are shown as a function of depth for each source-detector distance in Fig. 7. The responses decrease with increasing source depth and source-detector distance as expected. Apart from the 15 cm source depth, all MCNP responses converge within 10 % of measured counterparts.

Distributed source responses are shown as a function of source-detector distance for each source depth in Fig. 8. Strong convergence (within 3 %) was observed between the simulated and measured responses for all contamination scenarios in Fig. 8. Convergence levels increased linearly with increasing source-detector distance due to the solid angle effect: as the source-detector distance increases, the solid angle decreases. Hence, the number of photon pathways between the source and detector decreases, resulting in a lower margin of error for discrepancies between simulated and measured responses. It is important to note that it is not likely to encounter a distributed source that is perfectly uniform in the field. However, when compared to buried planar source responses, it was evident that more accurate estimates of realistic detector responses may be obtained with distributed source simulations, especially while further considering that uncertainties introduced from inhomogeneous soil density around a planar region are likely greater than those accumulated over a distributed region.

3.3. Application of ACFs and GSFs to idealized models

From Fig. 9, ACFs consistently decrease with increasing source-detector distance, suggesting that the effect of source area reduction on the ACFs is pronounced due to the solid angle effect.

Akin to Fig. 9, GSFs in Fig. 10 consistently decrease with source-detector distance once again due to the solid angle effect. Although, it appears that the total detector efficiency response is less sensitive to changes in clean soil cover thickness than source area reduction since the magnitudes of the GSFs are generally higher at each source-detector distance when compared to ACF counterparts.

In Fig. 11, planar source responses are shown for the idealized and modified cases, in addition to MCNP laboratory setup in comparison to the measured responses. Associated relative percent differences between simulated and measured responses are also provided in Fig. 12. Convergence between simulated and measured responses are shown to significantly improve in Fig. 12 after normalizing the ACFs/GSFs by the idealized responses. Nevertheless, we observe that the MCNP laboratory setup responses converge significantly more with measured counterparts when compared to the modified responses, which is primarily due to the following limitations. First, ACFs/GSFs do not account for other materials that may be present in the field aside from the soil, air, and detector (in this case, attenuation from the aluminum is absent). Second, planar source responses cannot be scaled to account for density since they are independent of source depth [37]. Third, ACFs/GSFs were calculated for cylindrical sources rather than planar. In Fig. 11, the latter limitation is shown to be insignificant when simulating infinitely wide sources since the response saturates for any given source-detector distance and source depth. However, this limitation was notably found to be significant for finite source areas after examining the standard MCNP output files. The combined impact of the aforementioned limitations on the responses in Fig. 11 increases with increasing source-detector distance (i.e., the responses decrease with source-detector distance and in turn become increasingly sensitive to the impact of all limitations). A sensitivity analysis would be required in subsequent work to quantify the impact of each of these limitations on the results.

In Fig. 13, distributed source responses are shown for the idealized and modified cases, in addition to MCNP laboratory setup in comparison to the measured responses. Associated relative percent differences between simulated and measured responses are also provided in Fig. 14. Akin to Fig. 12, significant improvements in levels of convergence between simulated and measured distributed source responses are shown in Fig. 14 after normalizing the idealized responses by the ACFs. The distributed source responses were, however, scaled to account for variations in soil density. The modified responses are consistently overestimated as evidenced by Figs. 13 and 14, mainly due to the absence of aluminum surrounding the soil in the models used to derive the ACFs.

3.4. Full energy peak detector efficiency analysis

Subtraction of the Compton continuum from each measured photopeak improves convergence between simulated and measured responses in Figs. 15-17. Uncertainties in the measured responses after subtraction are within 5 %, with the exception of the 32 cm source depth cases. High attenuation and low signal penetration resulted in poor statistics for the measured photopeak spectra for the 32 cm depth cases, which would require extensive sample counting times to obtain reliable photopeak responses which may be infeasible for field assay scenarios. For all remaining source depths and source-detector distances, the MCNP photopeak responses are underestimated from measured counterparts. Inclusion of GEB smoothing of the MCNP spectra slightly improved levels of convergence with measurements by more accurately representing the statistical distribution of the Gaussian photopeak. All simulated smoothed and unsmoothed ^{137}Cs spectra shown alongside measured counterparts are provided in Figs. A.1-A.12 in Appendix A: Supplementary Data.

It should be emphasized that use of the total detector efficiency may often be limited to measurements of simple radionuclide inventories (e.g., ^{137}Cs and ^{60}Co fallout deposited in soil); significant errors may be introduced when estimating radionuclide concentrations from complex inventories consisting of overlapping spectrum peaks. A higher resolution gamma detection system (e.g., HPGe-based) may be utilized in the field to initially identify radionuclide inventory constituents at a contaminated site prior to performing extensive surveying measurements with NaI(Tl)-based detection systems; however, the feasibility (i.e., inclusive of cost and maintenance) of alternative detection systems for large-scale radiological site remediation applications must be considered. Considering that the main limitation of *in-situ* gamma spectrometry is attributed to the determination of radionuclide depth distributions (i.e., source activity concentration as a function of depth) [21], the method of Whetstone and Kearfott [38] may be automated in future work – this may enable real-time, accurate determinations of radionuclide depth distributions in the field while also exploiting the portability and cost-effectiveness of NaI(Tl)-based detection systems. Moreover, the ACFs/GSFs and idealized calibration factors from this work may also be implemented in the RESidual RAdioactivity (RESRAD) code [39] to derive site-specific regulatory limits (given as CPM) in future applications.

4. Conclusions

Laboratory measurements were performed with a^{137}Cs field surrogate source term to validate simulated MC energy deposition-based (total and full energy peak) detector efficiencies (normalized to CPM), which may ultimately be used to facilitate large-scale radiological site remediation applications. When compared to simulated full energy peak detector efficiency responses, total detector efficiency responses were shown to consistently converge better with measured counterparts, mainly due to inherent difficulties in determining broadened spectra photopeak areas for NaI(Tl) detectors. Longer counting times are often required to obtain reliable full energy peak detector efficiency responses in comparison (especially for buried source depth profiles), potentially increasing field surveying efforts significantly. Additionally, newly derived ACFs and GSFs effectively modified the idealized total detector efficiency responses (used to derive baseline regulatory limits). While site-specific information may be needed to successfully demonstrate regulatory compliance in the radiological site remediation process, the simulated total detection efficiency from energy deposition in the active volume of the detector crystal can be adopted for radionuclide screening purposes.

CRediT authorship contribution statement

E. Asano: Data curation, Formal analysis, Investigation, Methodology, Validation, Visualization, Writing – original draft, Writing – review & editing. **S.A. Dewji:** Conceptualization, Data curation, Formal analysis, Investigation, Methodology, Project administration, Resources, Supervision, Validation, Writing – original draft, Writing – review & editing.

Declaration of competing interest

The authors declare that they have no known competing financial interests or personal relationships that could have appeared to influence the work reported in this paper.

Data availability

Data will be made available on request.

Acknowledgements

The authors would like to thank Vanessa Wei and Lotem Buchbinder Shadur of the RED^2 Laboratory for their assistance with assembling the experimental setups. The authors would also like to thank the Oak Ridge National Laboratory (ORNL) Nuclear Energy and Fuel Cycle Division (NEFCD) for the allocation of parallel computing resources.

Appendix A. Supplementary data

Supplementary data to this article can be found online at https://doi.org/10.1016/j.nima.2023.169067.

References

[1] ITRC (Interstate Technology and Regulatory Council), Real-time measurement of radionuclides in soil: technology and case studies. https://rais.ornl.gov/documents/RAD_4Web.pdf. (Accessed 19 October 2023).
[2] U.S. EPA, Multi-agency radiation survey and site investigation manual (MARSSIM). https://www.epa.gov/radiation/multi-agency-radiation-survey-and-site-investigation-manual-marssim. (Accessed 19 October 2023).
[3] E. Asano, et al., Photon detector response function methodology using MCNP and Shift hybrid radiation transport code for wide-area contamination assay applications, Nucl. Instrum. Methods Phys. Res. Sect. A Accel. Spectrom. Detect. Assoc. Equip. (2022) 1031.
[4] E. Asano, S. Dewji, (In Press) Effectiveness of Radiation Transport Variance Reduction Methods for Wide-Area Environmental Contamination Applications, Nucl. Sci. Eng. (2024).
[5] J. Wagner, A. Haghighat, Automated variance reduction of Monte Carlo shielding calculations using the discrete ordinates Adjoint function, Nucl. Sci. Eng. 128 (1998).
[6] C. Werner, et al., MCNP User's Manual - Code Version 6.2, 2022. Available at: https://mcnp.lanl.gov/pdf_files/TechReport_2017_LANL_LA-UR-17-29981_WernerArmstrongEtAl.pdf. (Accessed 19 October 2023).
[7] S. Johnson, et al., Omnibus User Manual, 2022. Available at: https://info.ornl.gov/sites/publications/Files/Pub120294.pdf. (Accessed 19 October 2023).
[8] T. Pandya, et al., Implementation, capabilities, and benchmarking of Shift, A massively parallel Monte Carlo radiation transport code, J. Comput. Phys. 308 (2016).
[9] D. Kocher, Dose-rate conversion factors for external exposure to photons and electrons, Health Phys. 45 (1983) 665–686.
[10] M. Bellamy, et al., Area correction factors for contaminated soil for use in risk and dose assessments. https://epa-bdcc.ornl.gov/Documents/ACF_FINAL.pdf. (Accessed 19 October 2023).
[11] M. Bellamy, et al., Gamma shielding factors for soil covered contamination for use in risk and dose assessments. https://epa-sdcc.ornl.gov/GSF_FINAL.pdf. (Accessed 19 October 2023).
[12] P. Jacob, et al., Effective dose equivalents for photon exposures from plane sources on the ground, Radiat. Protect. Dosim. 14 (1986) 299–310.
[13] U.S. EPA, Soil screening guidance for radionuclides: technical background document. https://nepis.epa.gov/Exe/ZyPDF.cgi/P100A0ZT.PDF?Dockey=P100A0ZT.PDF. (Accessed 19 October 2023).
[14] W. Lowder, H. Beck, W. Condon, Spectrometric determination of dose rates from natural and fall-out gamma-radiation in the United States, 1962-1963, Nature 202 (1064) (2023) 745–749.
[15] H. Beck, W. Condon, W. Lowder, Spectrometric techniques for measuring environmental gamma radiation. https://www.osti.gov/servlets/purl/4611888. (Accessed 19 October 2023).
[16] H. Beck, G. de Planque, The radiation field in air due to distributed gamma-ray sources in the ground. https://apps.dtic.mil/sti/pdfs/ADA382486.pdf. (Accessed 19 October 2023).

[17] K. Miller, et al., Radiation measurements following the Three Mile Island reactor accident. https://www.osti.gov/servlets/purl/6134501. (Accessed 19 October 2023).
[18] C. Gogolak, et al., Observations of the Chernobyl Fallout in Germany by in Situ Gamma-Ray Spectrometry, Compendium of Environmental Measurement Laboratory Research Projects Related to the Chernobyl Nuclear Accident, 1986, pp. 244–258.
[19] I. Helfer, K. Miller, Calibration factors for Ge detectors used for field spectrometry, Health Phys. 55 (1988) 15–29.
[20] International Commission on Radiation Units and Measurements (ICRU), Gamma-ray spectrometry in the environment. https://www.icru.org/report/gamma-ray-spectrometry-in-the-environment-report-53/. (Accessed 19 October 2023).
[21] R. Benke, K. Kearfott, An improved in situ method for determining depth distributions of gamma-ray emitting radionuclides, Nucl. Instrum. Methods Phys. Res. Sect. A Accel. Spectrom. Detect. Assoc. Equip. 463 (2001) 393–412.
[22] Mirion Technologies, NAIS-2x2™ nal(TI). https://www.mirion.com/products/technologies/spectroscopy-scientific-analysis/gamma-spectroscopy/detectors/scintillation-czt-detectors-accessories/nais-2x2-led-temperature-stabilized-scintillation-detector. (Accessed 19 October 2023).
[23] Mirion Technologies, Osprey. https://www.mirion.com/products/technologies/spectroscopy-scientific-analysis/gamma-spectroscopy/detector-electronics/osprey-universal-digital-mca-tube-base-for-scintillation-spectrometry. (Accessed 19 October 2023).
[24] Mirion technologies, Genie. https://www.mirion.com/products/technologies/spectroscopy-scientific-analysis/gamma-spectroscopy/gamma-spectroscopy-software/lab-applications/genie-spectroscopy-software-suite. (Accessed 19 October 2023).
[25] National Institute of Standards and Technology, Calibrated reference gamma button source (NIST serial number XYZ). https://www.nist.gov/gamma-source-XYZ, 2023. (Accessed 19 October 2023).
[26] K. Saito, P. Jacob, Gamma-ray fields in the air due to sources in the ground, Radiat. Protect. Dosim. 58 (1995) 29–45.
[27] U.S. EPA, Primer on radionuclides commonly found at Superfund sites. https://semspub.epa.gov/work/HQ/176328.pdf. (Accessed 19 October 2023).
[28] S. Smith, M. Lucas, Gamma-ray detectors, passive nondestructive assay of nuclear materials. https://sgp.fas.org/othergov/doe/lanl/docs1/00326398.pdf. (Accessed 19 October 2023).
[29] L. Carter, R. Schwarz, MCNP visual editor computer code manual. https://www.osti.gov/servlets/purl/88641. (Accessed 19 October 2023).
[30] Mirion technologies, 802 scintillation detectors. https://www.mirion.com/products/technologies/spectroscopy-scientific-analysis/gamma-spectroscopy/detectors/scintillation-czt-detectors-accessories/802-scintillation-detectors. (Accessed 19 October 2023).
[31] S. Philips, et al., ISOCS characterization of sodium iodide detectors for gamma-ray spectrometry. https://www.researchgate.net/publication/4154416_ISOCS_characterization_of_sodium_iodide_detectors_for_gamma-ray_spectrometry. (Accessed 19 October 2023).
[32] F. Fritsch, J. Butland, A method for constructing local monotone piecewise cubic interpolants, SIAM J. Sci. Comput. 5 (1984) 300–304.
[33] International Commission on Radiological Protection, Nuclear decay data for dosimetric calculations. https://www.icrp.org/publication.asp?id=ICRP%20Publication%20107. (Accessed 19 October 2023).
[34] A. Chilton, J. Shultis, R. Faw, Principles of Radiation Shielding, Prentice-Hall, Inc., Englewood Cliffs, New Jersey, 1984.
[35] S. Dewji, N. Hertel, A. Ansari, Assessing internal contamination after the detonation of a radiological dispersion device using A 2×2-inch sodium iodide detector, Radiat. Protect. Dosim. 155 (3) (2013) 300–316.
[36] U.S. NRC, Minimum detectable concentrations with typical radiation survey for instruments for various contaminants and field conditions. https://www.nrc.gov/docs/ML2023/ML20233A507.pdf. (Accessed 19 October 2023).
[37] S. Chen, Calculation of effective dose-equivalent responses for external exposure from residual photon emitters in soil, Health Phys. 60 (1991) 411–426.
[38] Z. Whetstone, S. Dewey, K. Kearfott, Simulation of a method for determining one-dimensional ^{137}Cs distribution using multiple gamma spectroscopic measurements with an adjustable cylindrical collimator and center shield, Appl. Radiat. Isot. 69 (2011) 790–802.
[39] C. Yu, et al., User's Manual for RESRAD Version 6, 2001. Available at: https://resrad.evs.anl.gov/docs/resrad6.pdf. (Accessed 19 October 2023).